

Laser ablation synthesis of C–Si–H-doped Co_{1-x}O with novel (hkl)-specific paracrystal, Co interlayer and lattice shuffling

Shang-Ju Hsu¹ · Shih-Siang Lin¹ · Yuyuan Zheng¹ · Pouyan Shen¹ · Shuei-Yuan Chen²

Received: 5 December 2015 / Accepted: 16 February 2016 / Published online: 14 March 2016
© Springer-Verlag Berlin Heidelberg 2016

Abstract C–Si–H-doped Co_{1-x}O particulates/nanocondensates of rocksalt-derived types were formed by pulsed laser ablation of metallic Co plate in tetraethyl orthosilicate and characterized by X-ray/electron diffraction and vibrational/optical spectroscopy. Such crystals were found to contain (001) paracrystal plate having defect cluster periodicity ca. 2.5 times that of the host lattice, and $1\text{D } 3x$ and $5x\{111\}$ commensurate superstructures along with (111) $(\text{Co}/\text{CoO})_n$ multilayer. The $(\text{Co}/\text{CoO})_n$ multilayer by (111)-specific faulting and oxygen diffusion is of interest to the synthesis of cermet, in particular giant magnetoresistance material, whereas the overall substances with characteristic vibration modes, binding energy and UV–visible absorptions (3.1 and 3.7 eV) may have potential photocatalytic applications.

1 Introduction

The motivation of this research is to synthesize C–Si–H-doped cobalt oxide by pulsed laser ablation (PLA) of metallic Co in a liquid of mild redox condition, i.e.,

tetraethyl orthosilicate (TEOS), so that novel (hkl)-specific paracrystalline distribution of defect clusters, Co interlayering and lattice shuffling of the rocksalt-type structure can be tailored and the accompanied optical property changes characterized.

Bulk Co_{1-x}O of rocksalt-type structure and $\text{Co}_{3-3x}\text{O}_4$ of spinel-type structure, with considerable extent of nonstoichiometry due to $\text{Co}^{3+}/\text{Co}^{2+}$ ratio, were known to have paracrystalline distribution of defect clusters when prepared by a sintering–annealing route in air without dopant [1] or doped with Zr^{4+} [2], and Mg^{2+} [3, 4], to tailor the interspacing of the defect clusters.

Nanosized Co_{1-x}O particles were reported to have negligible defect clusters when produced by PLA of metallic Co target in an oxygen background gas [5]. Whereas the Mg-doped Co_{1-x}O nanoparticles have tailored paracrystalline distribution of defect clusters (ca. 1.5- to 2-nm interspacing), internal compressive stress (up to ca. 2 GPa) and well-developed {100} faces for coalescence as (100) 26.6° twist boundary with a fair coincidence site lattice (CSL) when produced by PLA of bulk MgO– Co_{1-x}O alloys in air [6]. By contrast, paracrystal arrays following the $\sim\{111\}$ vicinal planes of the rocksalt-type host, i.e., {112} and {113} occurred for the Mg-doped Co_{1-x}O particles fabricated by PLA of powdery MgO–CoO solid solution in water [7]. Recently, PLA synthesis in aqueous solution under specified pH, O_2 concentration and laser parameters was used to produce cobalt oxide/hydroxide nanoparticles with tailored size, morphology and structure [8]. It was found that PLA of bulk Co in the presence and absence of O_2 in an aqueous solution initially produced CoO and $\beta\text{-Co}(\text{OH})_2$ nanoparticles, respectively, that finally transformed into spinel-type Co_3O_4 through oxidation and/or thermal decomposition [8]. It is of interest to explore further the defect nanostructures of cobalt oxide by

Electronic supplementary material The online version of this article (doi:10.1007/s00339-016-9813-4) contains supplementary material, which is available to authorized users.

✉ Shuei-Yuan Chen
steven@isu.edu.tw

¹ Department of Materials and Optoelectronic Science, National Sun Yat-sen University, Kaohsiung 80424, Taiwan, ROC

² Department of Mechanical and Automation Engineering, I-Shou University, Kaohsiung 84001, Taiwan, ROC

the PLA route in a liquid with suitable redox condition to retain the metal/metal oxide coexisting state, such as TEOS which has been used successfully for the PLA synthesis of ZnO/Zn core shell nanoparticles [9], C–H-doped TiO₂ anatase with epitaxial Ti and TiO nuclei [10] and even polyynes together with flexible Si–H-doped carbon nanoribbons [11].

Here, Si–C–H-doped Co_{1-x}O nanoparticles with paracrystal and special planar defects were synthesized by PLA of metallic Co plate in TEOS. We focused on (1) the domain shape and interspacing of the paracrystalline distribution of defect clusters, (2), (hkl)-specific commensurate superstructures, (3) novel (Co/CoO)_n multiple cermet layer intergrowth as of concern to giant magnetoresistance (GMR) research [12, 13] and (4) characteristic vibration, atom binding energy and UV–visible absorbance of the cermet particles retained in TEOS for potential photocatalytic applications. Such knowledge sheds light also on defect clustering and phase behavior of the Co–C–Si–O–H system in natural dynamic settings of gentle redox condition.

2 Experimental

Polycrystalline metallic Co plate of fcc- and hcp-type structures with negligible impurities (99.9 % pure) was subjected to energetic PLA (Nd–YAG-laser, Lotis, 1064 nm wavelength, beam mode: TEM00) under 1064 rather than 532 nm wavelength for a better ablation efficiency in TEOS. The upper surface of the target plate was 5 mm below the liquid level in a beaker of 6 cm in diameter full of TEOS ca. 15 cm³ in volume during such an ablation process. In such experiments, laser beam was focused to a spot size of 0.03 mm² on the target under laser pulse energy of 1000 mJ/pulse using 1064-nm excitation. The free-run mode for specified pulse duration of 240 μs was adopted to achieve a peak power density of 1.4×10^7 W/cm² (average power density 3.3×10^4 W/cm²) at 10 Hz. Under such a condition, Co target burning was avoided, whereas the reaction of TEOS with Co-containing plasma was effective to produce milligram-scale particulates/nanocondensates for phase, nanostructure and optical property characterizations. (The yield rate of the particulates/nanoparticles was estimated to be ca. 10 mg per 5 min of PLA accumulation time.)

The condensed and solidified particles along with tramp target debris produced by PLA of Co in TEOS for 5–10 min were centrifuged from the colloidal suspension and then deposited on a glass slide for X-ray diffraction (XRD, Bruker D8 Advance, Cu K_α at 40 kV, 40 mA and 3 s for each 0.05° increment from 20° to 90° of 2θ angle), optical microscopy under plane polarized light and scanning electron microscopic (SEM, JEOL JSM 6330F at

10 kV) observations. The composition and crystal structures of the fine particles collected on copper grids overlaid with a carbon-coated collodion film were further characterized by transmission electron microscopy (TEM, JEOL TEM-3010) coupled with bright-field image (BFI), selected area electron diffraction (SAED) and point-count energy dispersive X-ray (EDX) analysis at a beam size of 5 or 10 nm.

The UV–visible absorption of the colloidal suspension containing the as-formed particles was characterized by the instrument of U-3900H, Hitachi, with a resolution of 0.1 nm in the range of 190–900 nm. The vibration units of the carbonaceous and cobalt oxide substances as centrifuged from the colloidal suspension and then deposited on the glass slide were studied by Raman probe using HORIBA HR800 instrument at 633-nm laser excitation with a spatial resolution of 1 μm. The centrifuged condensates were also mixed with KBr for Fourier transform infrared spectroscopy (FTIR, Bruker 66v/S, 64 scans with 4 cm⁻¹ resolution) study of the cobalt oxide particles with Si–C–O–H signature. The colloidal suspension was also dropped onto glass substrate and then dried for X-ray photoelectron spectroscopy (XPS, JEOL JPS-9010MX photoelectron spectrometer with MgKα X-ray source) study calibrated with a standard of C1s at 284.5 eV [14].

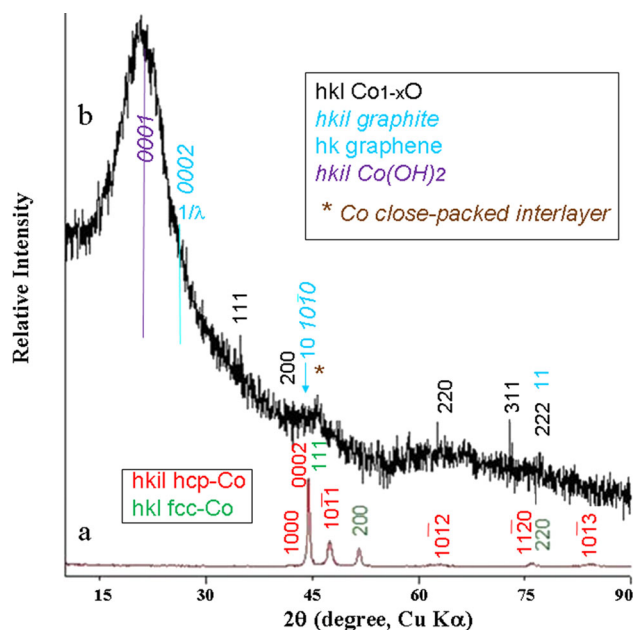


Fig. 1 XRD traces of *a* Co target with fcc- and hcp-type Co, *b* sample produced by PLA of Co in TEOS for 10 min to have the new phase assemblage including a unique (111) Co interlayer as denoted by asterisk

3 Results

3.1 XRD

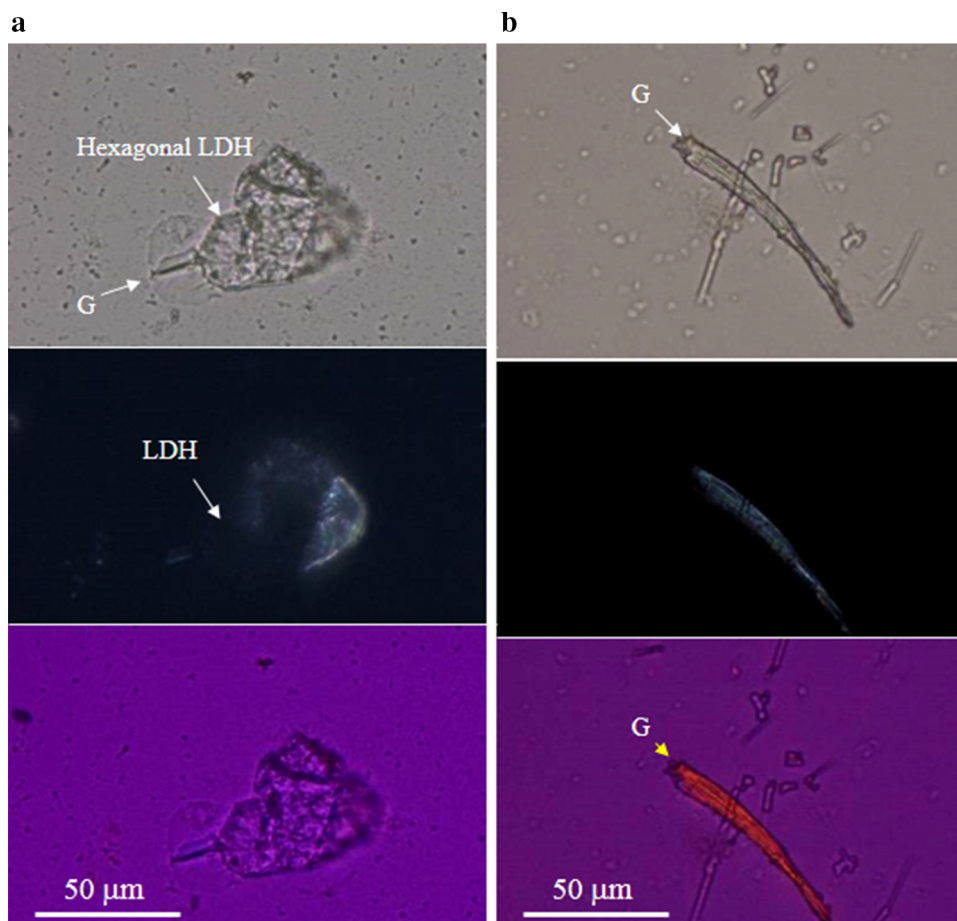
The metallic Co target is polycrystalline showing diffraction peaks of fcc- and hcp-type structures in random orientation (Fig. 1a). The sample in milligram scale produced by PLA of metallic Co in TEOS for 10 min showed a unique diffraction of (111) Co interlayer with 0.1983 nm (ca. $46.3^\circ 2\theta$, i.e., with ~ 0.45 -nm spacing when coupled with (111) CoO of 0.24602 nm (JCPDS 48-1719) as $(\text{Co}/\text{CoO})_n$ cermet bilayer as indicated by later TEM imaging), besides the weak diffractions of Co_{1-x}O . This (111) Co interlayer spacing is in close agreement with that of bulk fcc Co without dopant (0.19745 nm, JCPDS 88-2325). There is minor $\text{Co}(\text{OH})_2$ layer double hydroxide (LDH) with basal diffraction superimposed with the broad diffraction of silica glass substrate at ca. $20^\circ 2\theta$ and additional carbon in the form of turbostratic graphene and graphite to give weak basal and prism diffractions.

3.2 Optical polarized microscopy and SEM

Optical polarized micrographs taken from two areas of the sample produced by PLA of metallic Co in TEOS for 5 min and then collected on a silica glass slide showed that the C–Si–H-doped Co_{1-x}O particles are nano to microns in size, in drastic contrast to the much larger-sized $\text{Co}(\text{OH})_2$ LDH with hexagonal shape and the turbostratic graphene in tubular form (Fig. 2). The hexagonal LDH in basal section showed full extinction, whereas the tubular graphene showed a high refraction index along the long axis, i.e., length slow, under crossed polarizers with additional λ -plate.

SEM–EDX analysis (Fig. 3) of the same PLA specimen showed that the graphene tube was Si–O–H-doped and decorated with Co_{1-x}O particulates/nanocondensates agglomerated as chain aggregate or in a close-packed manner. The C–Si–H-doped Co_{1-x}O also occurred as spherical particulate up to ca. 2 μm in size which is much brighter than the graphite flake nearby (Fig. 4). It is noteworthy that the spherical particulate has local facets presumably due to coalescence of the constituent faceted

Fig. 2 Optical polarized micrographs of the particulates and condensates (mainly C–Si–H-doped Co_{1-x}O , hexagonal LDH and graphene) in two areas (a) and (b) produced by PLA of Co in TEOS for 5 min, taken under open polarizer (*upper panel*), crossed polarizers (*middle panel*) and crossed polarizers with additional λ -plate (*lower panel*) showing length slow of the elongated graphene belt/tubes and extinction of the hexagonal LDH in isotropic section



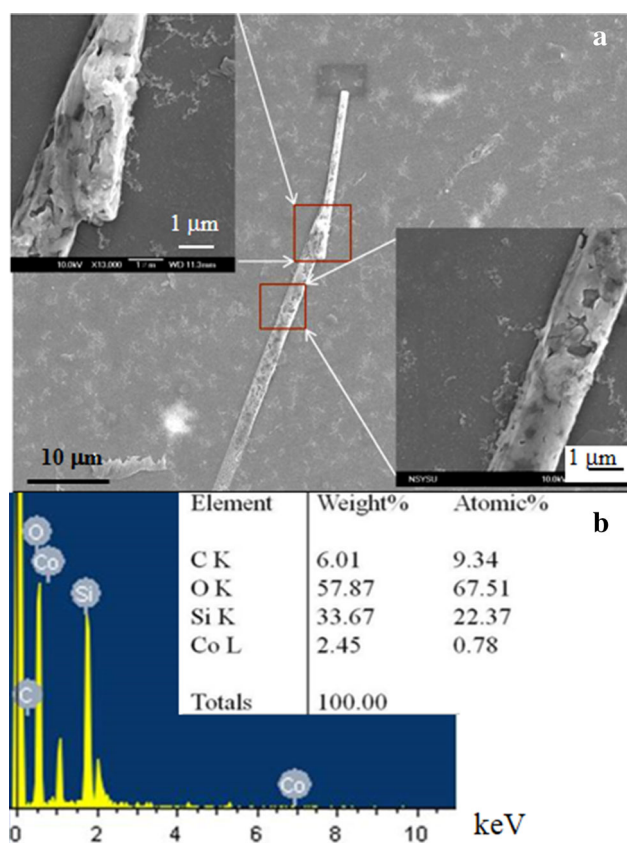


Fig. 3 SEM **a** SEI and **b** EDX spectrum of the Si–O–H-doped graphene rod produced by PLA of Co in TEOS for 5 min having Si and O counts from the glass substrate and Co counts from the decorated Co_{1-x}O particulates and nanocondensates

particles, whereas the graphite flake has perfect hexagonal shape rather than the turbostratic stacking of graphene.

3.3 TEM

3.3.1 Size distribution and cell parameter of C–Si–H-doped Co_{1-x}O

TEM BFI and corresponding SAED pattern of the sample produced by PLA of Co in TEOS for 10 min (Fig. 5) showed characteristic diffraction rings of C–Si–H-doped Co_{1-x}O particulates and nanocondensates ranging from 5 to 40 nm in size in random orientation and a unique (111)(Co/CoO)_n diffraction nearly superimposed with the graphene (10) and/or graphite (10 $\bar{1}$ 0) diffraction as a combined broad diffraction ring. Depending on the orientation, the C–Si–H-doped Co_{1-x}O particulates and nanocondensates showed planar defects which are in fact (111)-specific faults and (111)(Co/CoO)_n cermet interlayers as addressed later. On the basis of the observed and then refined *d*-spacings of the diffraction rings in Fig. 5, the lattice parameter of the

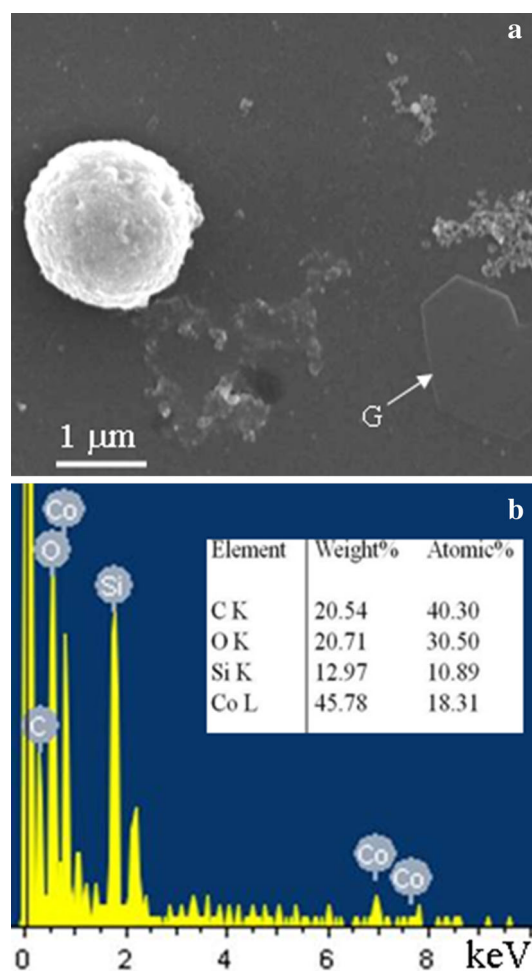


Fig. 4 SEM **a** SEI and **b** EDX spectrum of a typical spherical C–Si–H-doped Co_{1-x}O particulate produced by PLA of Co in TEOS for 5 min. Note the nearby graphite (G) flake with almost perfect hexagonal shape

rocksalt-type C–Si–H-doped Co_{1-x}O nanocondensates was determined as 0.401 ± 0.002 nm which is significantly smaller than undoped CoO in bulk (0.42610 nm, JCPDS 48-1719) as compiled in Table 1. The larger-sized C–Si–H-doped Co_{1-x}O particulate however has a larger cell parameter (0.430 ± 0.002 nm) based on the structure refinement of a typical particulate in the [001] zone axis (Supplement Figure 1) as compiled in Table 2. Such lattice parameter difference is due to competing factors of internal compressive stress and dopant content as addressed later.

3.3.2 Shape and special grain boundaries of C–Si–H-doped Co_{1-x}O

The BFI, DFI and SAED pattern (Fig. 6a–c) of an abnormal large-sized (ca. 0.1 μm in diameter) spherical C–Si–H-

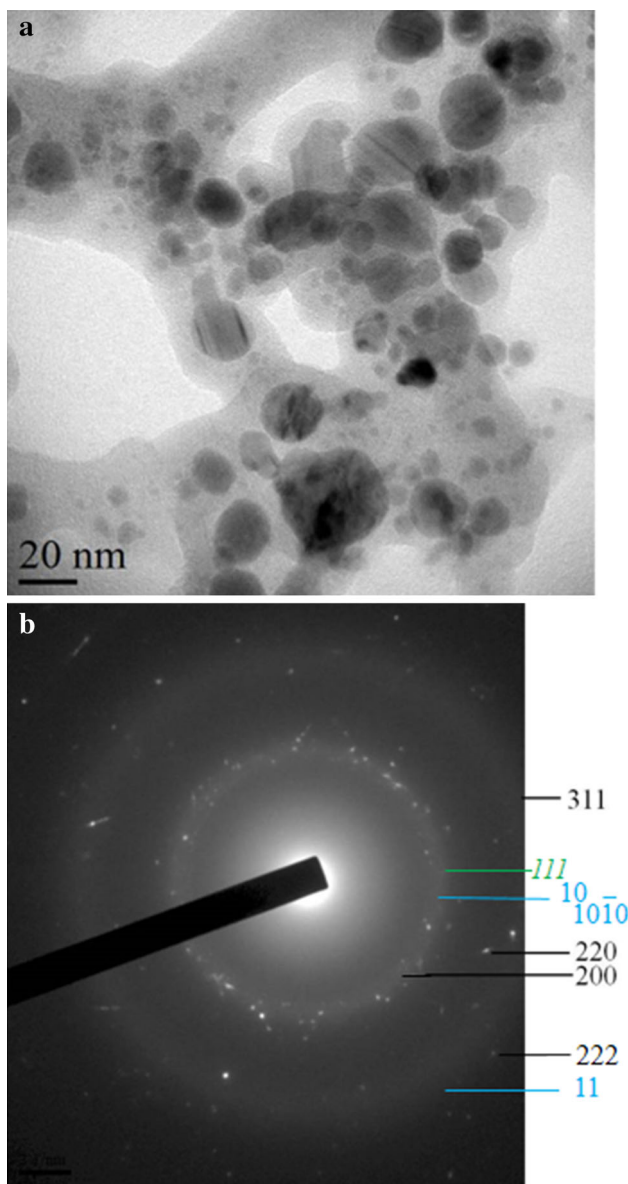


Fig. 5 TEM **a** BFI and **b** SAED pattern of C–Si–H-doped Co_{1-x}O particulates and nanocondensates produced by PLA of Co in TEOS for 10 min. Note weak diffractions of graphite (hkil), graphene (hk) and (111) interlayer of Co (cf. text)

doped Co_{1-x}O particulate in the [001] zone axis produced by PLA of Co in TEOS for 5 min showed diffraction splitting of slightly misoriented upper left and lower right parts. Such a slight misorientation can be attributed to almost oriented attachment of two particles over their originally imperfect (100) surfaces, now a small-angle [001] (100) symmetrical tilt boundary.

Figure 7a–d shows the BFI, DFI, SAED pattern and EDX spectrum of another C–Si–H-doped Co_{1-x}O particulate ca. 40 nm in size in the [011] zone axis, indicating that

Table 1 Observed and refined *d*-spacings (± 0.002 nm) for lattice parameter refinement of C–Si–H-doped Co_{1-x}O nanocondensates based on electron diffraction rings in Fig. 5

(hkl)	Observed (nm)	Refined (nm)	Undoped CoO JCPDS 48-1719
200	0.199	0.201	0.21307
220	0.141	0.142	0.15066
311	0.125	0.121	0.12848
<i>a</i>		0.401	0.42610
<i>V</i> (nm ³)		0.065	0.07737

it was composed of (hkl)-specific coalesced nanoparticles with $\sim(100)$ and $\{111\}$ facets and a high angle grain boundary, as indicated by extra (111) diffraction, due to arbitrary coalescence.

3.3.3 Paracrystal and (111)-specific defects of C–Si–H-doped Co_{1-x}O

Lattice image coupled with 2D forward and inverse Fourier transform (Fig. 8a–c) of a nearly spherical C–Si–H-doped Co_{1-x}O particulate ca. 40 nm in size in the [001] zone axis showed (001) disk-like domains with paracrystalline distribution of defect clusters in a rather regular manner having interspacing ca. 2.5 times the lattice parameter of the rocksalt-type host.

The C–Si–H-doped Co_{1-x}O particulate also showed close-packed Co interlayer alternatively mixed with the (1 $\bar{1}$ 1) layer of the host, i.e., the (1 $\bar{1}$ 1)(Co/CoO)_{*n*} bilayer in multiple with ca. 0.45-nm interspacing as indicated by BFI, DFI, SAED pattern (Fig. 9a–c) and an enlarged DFI using (1 $\bar{1}$ 1) diffraction spot of a nearly spherical particulate ca. 60 nm in size coupled with a schematic drawing of atoms in the [$\bar{1}$ 12] zone axis (Fig. 9d). It should be noted that the (111)Co layer was manifested by the diffraction spot but cannot be resolved in real space unless coupled with the (111)CoO layer to show the fringes with ca. 0.45-nm interspacing. Not also that the (1 $\bar{1}$ 1)(Co/CoO)_{*n*} cermet multiple layers do not have the ABC stacking order of the fcc-type Co as otherwise the corresponding diffraction of the fcc-type should show up along the [110] reciprocal direction in the [$\bar{1}$ 12] zone axis.

There are other (111)-specific defects, i.e., 1D 5x(1 $\bar{1}$ 1) and 3x(1 $\bar{1}$ 1) commensurate superstructures as manifested by the lattice image (Fig. 10a) coupled with 2D forward and inverse Fourier transform from regions I and II of two separated C–Si–H-doped Co_{1-x}O particulates near the [$\bar{1}$ 12] and [011] zone axis, respectively (Fig. 10b, c). There are Moiré fringes due to superimposed phases in the case of Fig. 10b.

Table 2 Observed and refined d -spacings (± 0.002 nm) for lattice parameter refinement of C–Si–H-doped Co_{1-x}O particulate based on electron diffraction spots in the $[001]$ zone axis (Supplement Figure 1)

(hkl)	Observed (nm)	Refined (nm)	Undoped CoO JCPDS 48-1719
200	0.215	0.215	0.21307
220	0.152	0.152	0.15066
400	0.108	0.107	0.10653
420	0.096	0.096	0.09529
a		0.430	0.42610
V (nm ³)		0.0793	0.07737

3.3.4 $\text{Co}(\text{OH})_2$ matrix

TEM lattice image coupled with 2D forward and inverse Fourier transform in Fig. 11 showed further that the 1D $5x(1\bar{1}1)$ faulted particulate in Fig. 10b is surrounded by the $\text{Co}(\text{OH})_2$ LDH matrix in the $[2\bar{1}\bar{1}0]$ zone axis having no epitaxial relationship with each other as indicated by the misaligned (0002) and $(1\bar{1}1)$ fringes.

3.4 Vibrational spectroscopy

The Raman probe of the two areas with enriched Si–H-doped Co_{1-x}O and amorphous silica are shown in Fig. 12a, b, respectively, for the sample produced by PLA of metallic Co in TEOS for 10 min, where the Co–O and Co–OH vibration units of CoO, Co_3O_4 and CoOOH refer to Ref. [15] and the 1105 cm^{-1} band can be assigned to amorphous Co–Si–O–H phase with Si_2O_5 cluster units analogous to that of gel-derived amorphous Zn_2SiO_4 [16].

The corresponding FTIR spectrum of the sample (Fig. 12c) showed characteristic absorbance bands of the structure units after the assignments of analogous materials by other investigators [17–20] as compiled in Table 3.

3.5 XPS

The XPS spectra of the C–Si–H-doped Co_{1-x}O along with minor LDH, graphene/graphite and amorphous silica produced by PLA of metallic Co in TEOS for 10 min showed binding energies of O1s, C1s, Si2p and Co2p under the influence of Si–O, Co–O, C–C, C–O, C=O linkages as indicated by Lorentzian–Gaussian curve fitting of the atom pairs (Fig. 13) calibrated with a standard of C1s at 284.5 eV [14]. The vague and broad Co2p peak at ca. 768–774 eV (Fig. 13d) would be contributed partly from thin Co interlayer, besides the effects of composition/charge variations and internal stress of the nanocondensates. In this regard, the Co2p spectra presented in the literature have controversial fittings and the standard cobalt

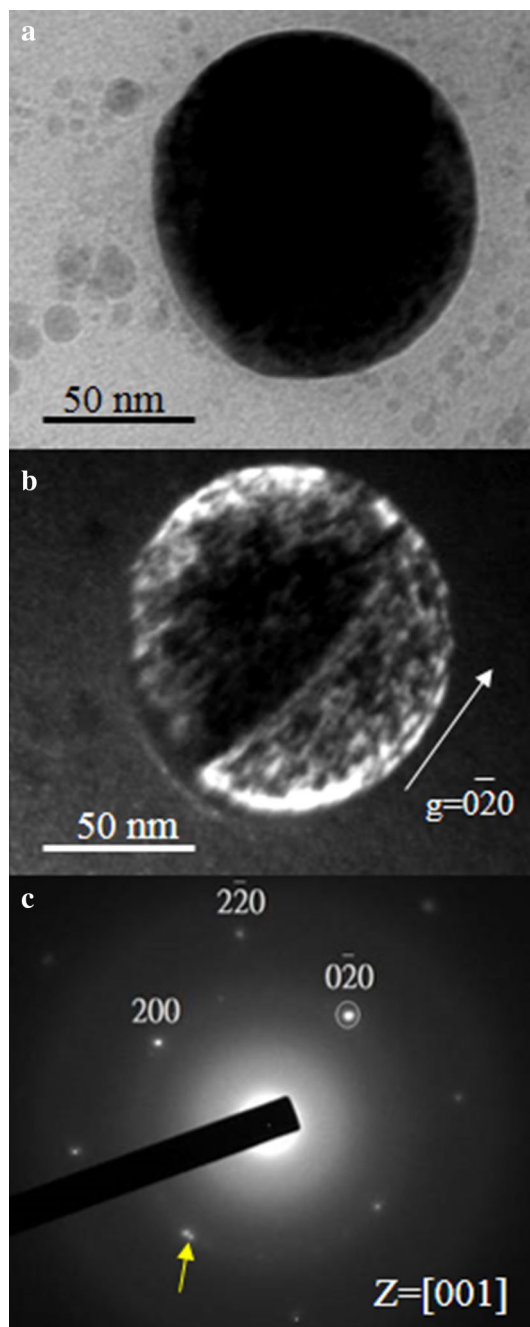
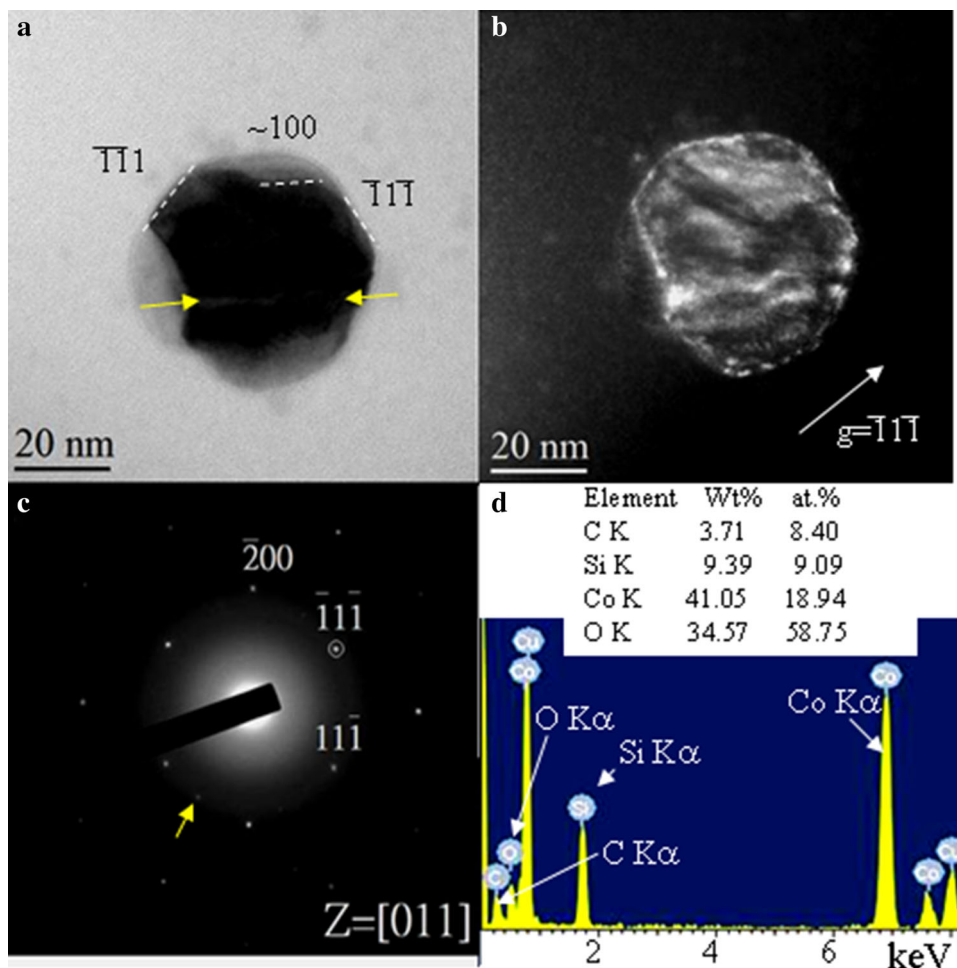


Fig. 6 TEM **a** BFI, **b** DFI and **c** SAED pattern of a spherical C–Si–H-doped Co_{1-x}O particulate with abnormal large size produced by PLA of Co in TEOS for 5 min. Note diffraction splitting (arrow) indicating slight misorientation of the upper left and lower right parts due to oriented attachment over their originally imperfect (100) surfaces

metal sample has a Co2p peak at 778.1 eV (cf. Table 5 of Ref. [21]). (As quoted from Ref. [21]: There appears to be few instances of good quality high resolution Co2p spectra presented in the literature. Fitting appears to be inconsistent with generally only a qualitative approach to the

Fig. 7 TEM **a** BFI, **b** DFI, **c** SAED pattern and **d** EDX spectrum of a typical C–Si–H-doped Co_{1-x}O particulate with $\sim(100)$ and $\{111\}$ facets, and high angle grain boundary to give extra (111) diffraction (arrow)



analysis of the spectral changes reported. Fitting of a broad main peak combined with a portion of the satellite structure has been one approach [22, 23], although fitting parameter details are not presented in enough detail to emulate. Recent work [24] has clarified the position and type of plasmon loss structure associated with the Co metal (and CoP, cobalt phosphide) spectrum. The Co metal spectrum is fitted with an asymmetric main peak and two plasmon loss peaks at 3.0 and 5.0 eV, which constitute the surface and bulk plasmons, respectively, with FWHM values of 3.0 eV in both cases.)

3.6 UV–visible absorbance

The UV–visible absorption spectrum of the colloidal suspension containing the particulates/condensates of Si–H-doped Co_{1-x}O as well as minor LDH, graphene and graphite as produced by PLA of metallic Co in TEOS for 5 min showed bimodal absorbance with extrapolations to the base line at 334 and 397 nm corresponding to a minimum band gap of 3.7 and 3.1 eV, respectively (Fig. 14).

4 Discussion

4.1 Phase selection by PLA of Co in TEOS

The rocksalt-type Co_{1-x}O was known to transform spontaneously into Co_3O_4 spinel when cooled below ca. 900 °C in open air or with oxygen partial pressure of 10^{-3} Pa [25]. By contrast, Si–C–H-doped Co_{1-x}O was retained to ambient condition by PLA of metallic Co in TEOS in the present study.

Apparently, the composition stabilization effect by the Si–C–H dopant accounts for the formation and retention of the rocksalt-type cobalt oxide in TEOS. Alternatively, the $\text{CoO}/\text{Co}_3\text{O}_4$ phase boundary may have a negative Clausius–Clapeyron ($\Delta T/\Delta P$) slope in order to have the rocksalt-type structure formed at high-temperature and high-pressure during the PLA process and then quenched to ambient condition. Still, the internal compressive stress by the PLA process was not high enough to form the Co_2SiO_4 spinel compound which was known to stabilize above 6 GPa at temperatures ([26], cf. also Fig. 4.19 of Ref. [27])

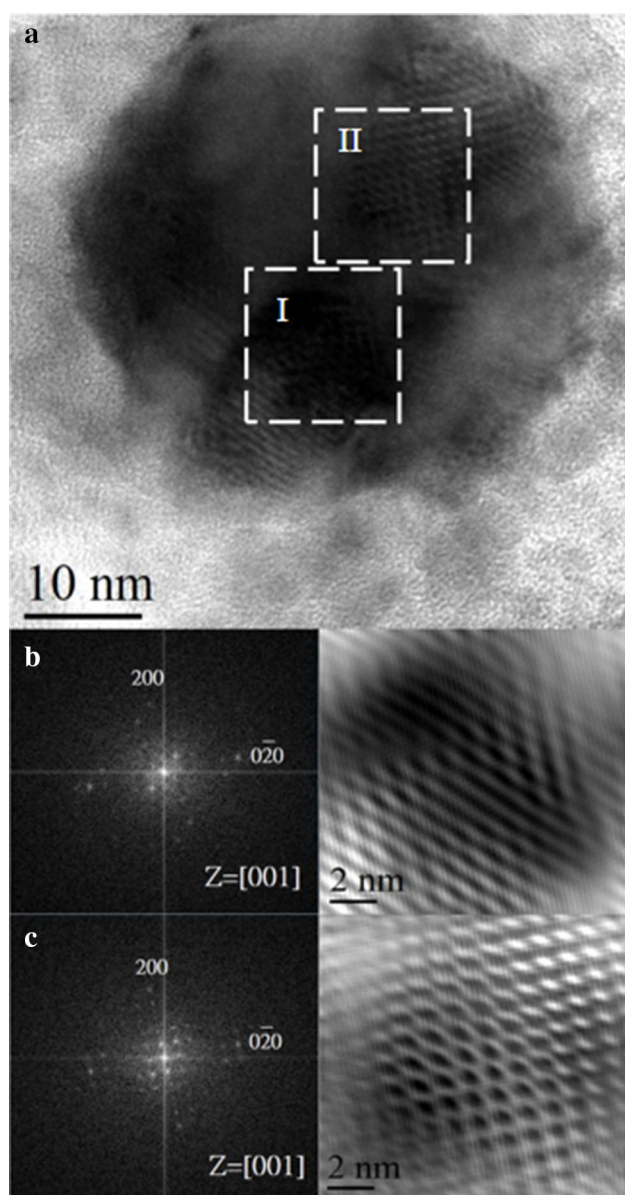


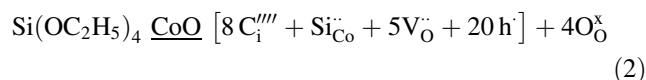
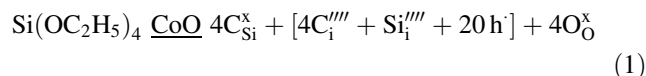
Fig. 8 TEM **a** lattice image; **b**, **c** 2D forward and inverse Fourier transform from the square regions I and II, respectively, of a typical C–Si–H-doped Co_{1-x}O particulate with paracrystalline distribution of defect clusters in a rather regular manner with ca. 2.5 times that of the host lattice parameter (cf. text)

although the kinetics of CoO and SiO_2 reaction to form compound is also of concern. The abundant $(111)(\text{Co}/\text{CoO})_n$ bilayer in multiple within the C–Si–H-doped Co_{1-x}O as manifested by the XRD and TEM results further indicates that metallic Co may also play a role on the stabilization of rocksalt- rather than spinel-type cobalt oxide. It is noteworthy that the Co-rich plume by the present PLA process in TEOS has consumed hydrocarbons to

circumvent the formation of polyynes which was largely produced by PLA of graphite in TEOS and remained intact upon prolonged dwelling in TEOS at room condition [11].

4.2 Defect chemistry and ordering scheme of C–Si–H-doped Co_{1-x}O

The TEOS-derived C–Si–H dopant for rocksalt-type cobalt oxide, as manifested by the combined electron diffraction and FTIR/Raman and XPS evidences, would involve the following defect chemistry equations in Kröger–Vink notation [28]:



where $\text{C}_i^{\prime\prime\prime\prime}$ and $\text{Si}_i^{\prime\prime\prime\prime}$ denote quarter valent carbon and silicon ions in the interstitial tetrahedral and/or octahedral sites charge-balanced by electron hole h^{\cdot} , i.e., proton, whereas $\text{Si}_{\text{Co}}^{\cdot\cdot}$ denotes Si^{4+} in substitution of Co^{2+} in octahedral sites charge compensated by the oxygen vacancy $\text{V}_{\text{O}}^{\cdot\cdot}$. The interstitial carbon and silicon dopants account for a significantly larger lattice parameter ($a_o = 0.430 \pm 0.002$ nm based on the refined d -spacings measured from the diffractions spots in the $[001]$ zone axis in Supplement Figure 1; cf. Table 2) than the ambient value of undoped CoO in bulk ($a_o = 0.42610$ nm, JCPDS file 48-1719) despite the internal compressive stress commonly retained for the small-sized particles of metal oxides produced by a dynamic PLA route as mentioned. Note the intergrowth of $(111)(\text{Co}/\text{CoO})_n$ cermet implies that the Si–C–H-doped rocksalt-type host may in fact be oxygen rather than cobalt deficient, i.e., CoO_{1-x} not Co_{1-x}O in accordance with the defect chemistry Eq. (2) rather than (1) to have a smaller cell parameter ($a_o = 0.401 \pm 0.002$ nm based on the refined d -spacings measured from the diffraction rings in Fig. 5; cf. Table 1) for the Si–C–H-doped cobalt oxide nanocondensates with (111) cermet interlayer.

The C–Si–H-doped Co_{1-x}O with paracrystal and (111) -specific defects, i.e., $1\text{D } 3x$ and $5x\{111\}$ commensurate superstructures and $(\text{Co}/\text{CoO})_n$ multilayer apparently have different ordering scheme from the spinelloids in the $\text{NiO}-\text{Al}_2\text{O}_3-\text{SiO}_2$ system [29, 30] or other composition systems (cf. Ref. [31] and references cited herein) having the spinel host $\langle 110 \rangle$ axes as the new principal axes of the orthorhombic and tetragonal derivatives. This indicates that the present paracrystal and (111) -specific superstructure have nothing to do with the spinelloid-based β -phase intermediate of the olivine \rightarrow spinel-type transition as

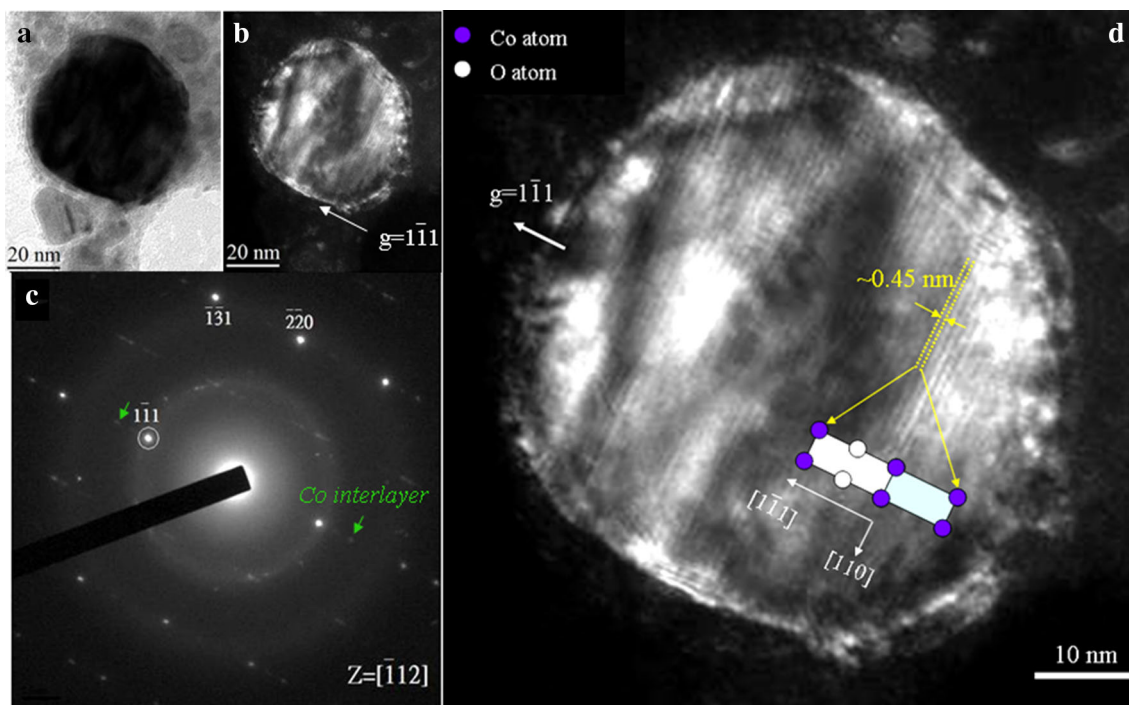


Fig. 9 TEM **a** BFI, **b** DFI, **c** SAED pattern and **d** enlarged DFI of a typical C–Si–H-doped Co_{1-x}O particulate with close-packed Co interlayer alternatively mixed with the $(\bar{1}\bar{1}\bar{1})$ layer of the host as indicated by the schematic drawing of atoms in the $[\bar{1}\bar{1}\bar{2}]$ zone axis (cf. text)

reported for Ni_2SiO_4 in the $\text{NiO–Al}_2\text{O}_3\text{–SiO}_2$ system [29, 30]. In any case, the defect clusters as a result of dopant from TEOS would be 3D distributed to form paracrystal (Fig. 8), whereas (111) -specific for the formation of planar defects (Fig. 10).

4.3 Formation mechanism of (111) -specific cermet interlayer in Co_{1-x}O

The cobalt oxide by the present PLA process in TEOS apparently is under suitable redox condition to retain the metal/metal oxide coexisting state as $(111)(\text{Co}/\text{CoO})_n$ bilayer in multiple, which is an interesting comparison with the ZnO/Zn core shell nanoparticles [9] and C–H-doped TiO_2 anatase with epitaxial Ti and TiO nuclei inclusions [10]. The reasons of forming $(111)(\text{Co}/\text{CoO})_n$ cermet interlayer are twofold.

Thermodynamically, the $(111)(\text{Co}/\text{CoO})_n$ cermet interlayers with fair coherency at the multiple interfaces may have beneficial lower strain energy analogous to polysynthetic twinings in metal alloys [32, 33] and a number of ceramics/minerals [34, 35]. The relief of ordering strain by twinning in bulk Ni–Mn alloy as proposed in ref [32] accounts for the polysynthetic twinning lamellae in many bulk metals alloys of fcc- and L1_2 -type structure such as FeNi_3 [33], and plagioclase minerals [34, 35] upon cooling

in natural occurrences. The (111) polysynthetic twinning also occurred in fcc-type AuCu_3 nanocondensates and particulates produced by PLA of AuCu in vacuum [36].

Kinetically, the close-packed (111) plane of fcc metal and rocksalt-type metal oxide may be the short circuit for inward/outward diffusion of oxygen atoms analogous to the case of epitaxial growth of Ti/TiC diffusion couple under an applied concentration gradient [37] or TiC/Ti₂C/graphene composite nanocondensates by PLA of TiC in vacuum [38]. It is also possible to have 1D $2\times(111)$ crystallographic shear faulting along the close-packed (111) planes of fcc Co metal by the PLA process for short-circuit inward oxygen diffusion upon radiant heating of the laser pulses. This is analogous to the case of shock-induced shuffling by the close-packed (110) planes of bcc crystal to form C-overdoped W nanocondensates of distorted body-centered orthorhombic type with 1D $2\times(110)$ commensurate superstructure by the PLA process in vacuum [39].

4.4 Implications

The rocksalt-type C–Si–H-doped Co_{1-x}O particulates/nanocondensates along with platy graphite and tubular turbostratic graphene/ $\text{Co}(\text{OH})_2$, as produced by PLA of metallic Co under gentle redox condition of TEOS, shed light on their occurrence in natural dynamic settings such

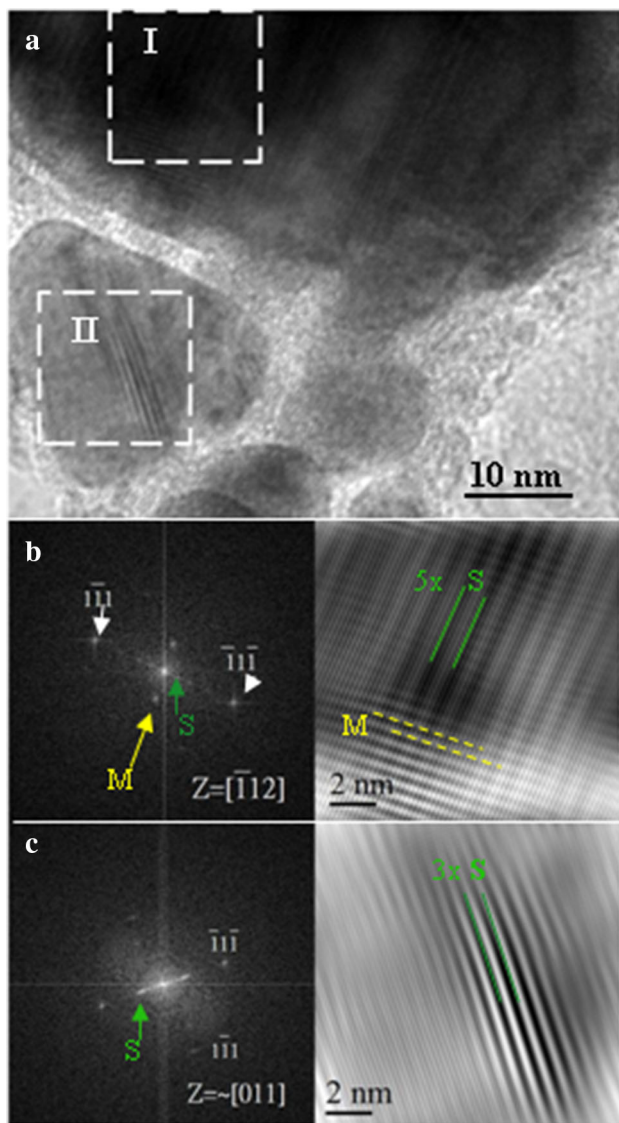


Fig. 10 TEM **a** lattice image; **b, c** 2D forward and inverse Fourier transform from regions I and II of two C-Si-H-doped Co_{1-x}O particulates, showing 1D $5x(1\bar{1}1)$ and $3x(1\bar{1}1)$ commensurate faulting superstructure (S), near the $[\bar{1}12]$ and $[011]$ zone axis, respectively. Note also Moiré fringes (M) due to superimposed phase in (b). The same area as in Fig. 9a

as that experienced by the planetary materials [40], and terrestrial lightening or impact sites rich in Co-C-Si-O-H component.

From engineering viewpoint, the C-Si-H-doped Co_{1-x}O particulates/nanocondensates with (001) platy domains of paracrystal and (111)-specific defects, i.e., 1D $3x$ and $5x\{111\}$ commensurate superstructures and $(\text{Co}/\text{CoO})_n$ multilayer are expected to have interesting physical chemical properties. It is of interest to note that the (111)-

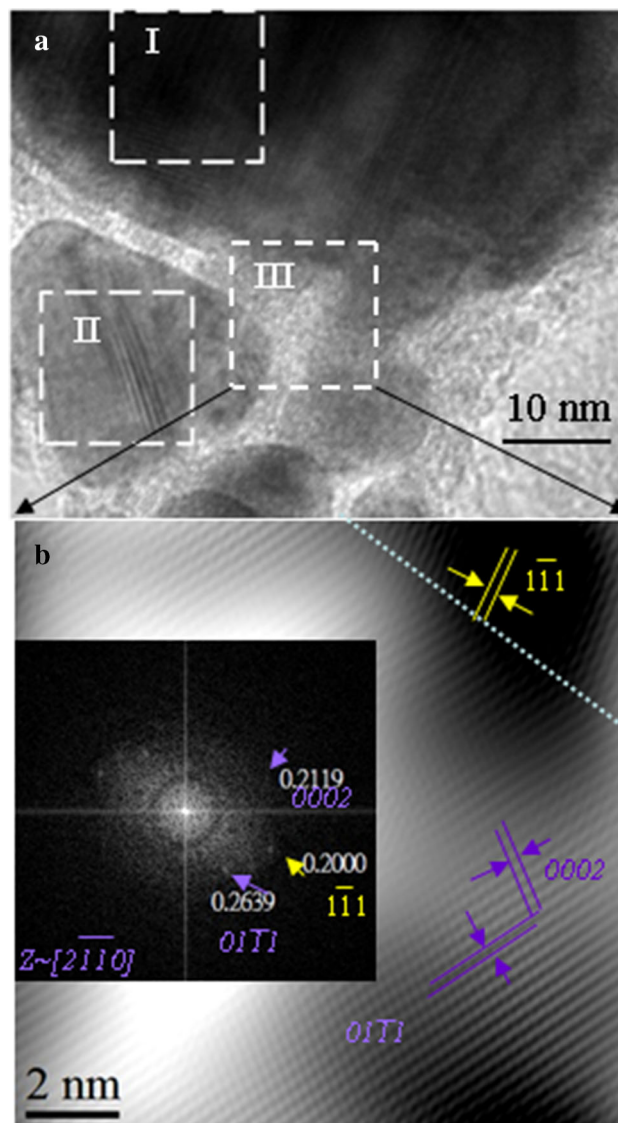


Fig. 11 TEM **a** lattice image, **b** 2D forward (*inset*) and inverse Fourier transform from region III, showing the $\text{Co}(\text{OH})_2$ LDH matrix in the $[2\bar{1}10]$ zone axis having no epitaxial relationship with the nearby C-Si-H-doped Co_{1-x}O particulate as indicated by the misaligned (0002) and $(1\bar{1}1)$ fringes with d -spacings as denoted in nanometer. The same area as in Fig. 9a

specific $(\text{Co}/\text{CoO})_n$ multilayer with ferromagnetic Co and nonmagnetic CoO atomic layers alternatively stacked may have enhanced magnetoresistivities, i.e., GMR analogous to original multilayer $(\text{Fe}/\text{Cr})_n$ [12], or trilayer Fe/Cr/Fe system [13] and later Co/Cu/Co trilayer pillars [41, 42] for potential magnetoelectronics or so-called spintronics applications such as read-out heads for magnetic disks and as sensor of magnetic fields. Future study of the epitaxial

Fig. 12 **a, b** Raman spectra taken from area with enriched Si–H-doped Co_{1-x}O and amorphous silica, respectively, and **c** FTIR spectrum of the sample produced by PLA of Co in TEOS for 10 min

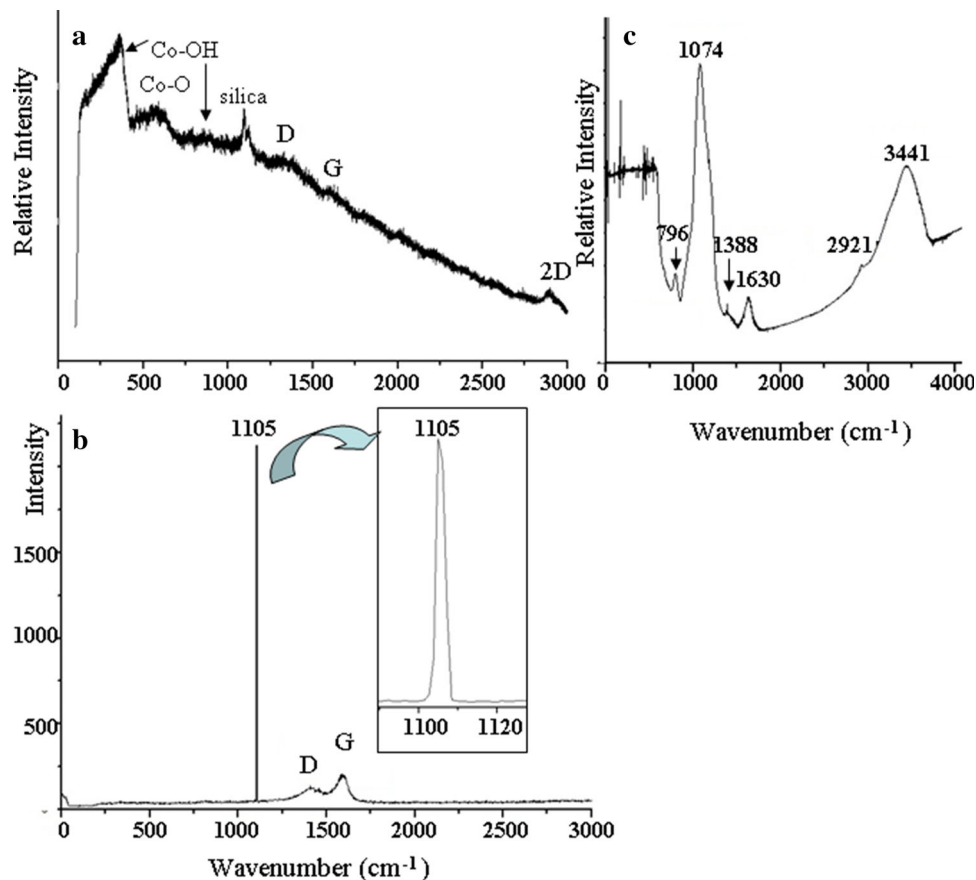


Table 3 Observed IR bands (Fig. 13c) and corresponding structure units in view of previous assignment to relevant materials (cf. text)

Observed (cm ⁻¹)	Vibrations	References
795.8	Si–O–Si stretching	[18]
1073.7	Si–O–Si stretching Asym C–O	[18]
1388.3	Sym C–H bending	[17]
1629.7	H–O–H bending	[19]
2921.4	Asym C–H stretching	[20]
3440.8	O–H stretching	[19]

Co/CoO superlattice sputtering deposited on a suitable substrate is of interest to see whether thickness miniature down to atomic layer for the (111)(Co/CoO)_n multilayer affects significantly the electron spin–orbital coupling behavior and hence the GMR and tunneling magnetic resistance (TMR) effect like barriers Fe/MgO/Fe

having been shown to have TMR values exceeding 200 % [43–45]. Furthermore, the overall substances of C–Si–H-doped Co_{1-x}O, graphene and Co(OH)₂ produced by the present PLA process in TEOS have multiple absorptions in UV–visible range (3.1–3.7 eV) for potential photocatalytic applications.

5 Conclusions

In this article, C–Si–H-doped Co_{1-x}O particulates/nanocondensates with (hkl)-specific paracrystal, Co interlayer and lattice shuffling in rocksalt-type structure, rather than Co₂SiO₄ spinel, were shown to form by PLA of Co plate in TEOS. The (001) platy paracrystal has defect cluster inter-spacing ca. 2.5 times the rocksalt-type lattice parameter. Whereas (111)-specific commensurate faulting and oxygen diffusion account for the 1D 3x and 5x(111) commensurate superstructures and (111) (Co/CoO)_n multilayer intergrowth. Further study is required to find out whether this mechanism

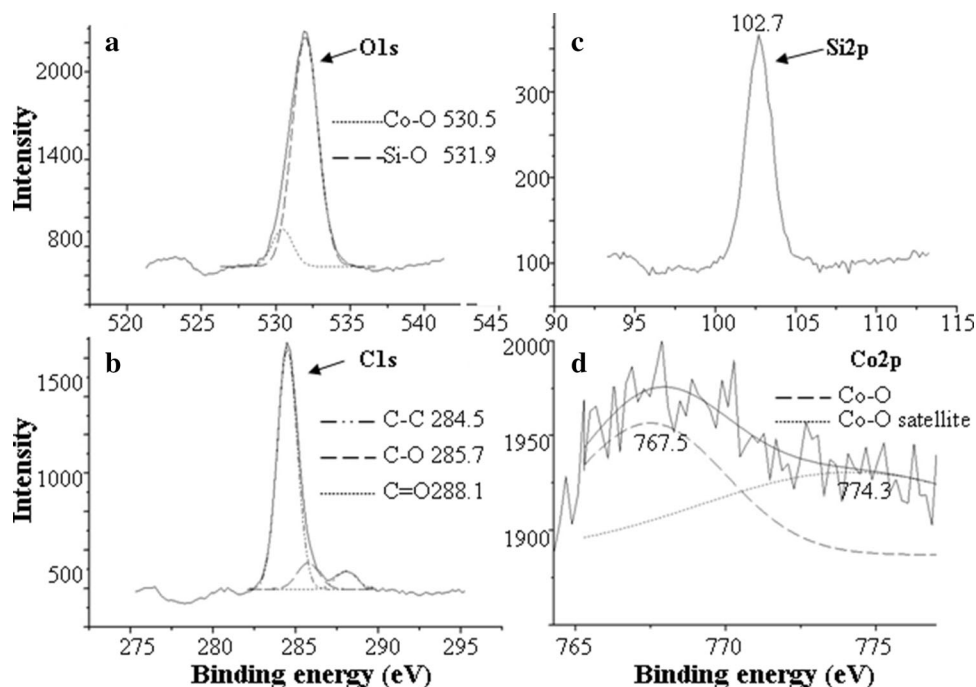


Fig. 13 XPS spectra of the condensates (mainly Si-H-doped Co_{1-x}O and minor LDH, graphene/graphite and amorphous silica) produced by PLA of Co in TEOS for 10 min showing binding energies of

a O1s, **b** C1s, **c** Si2p and **d** vague Co2p under the influence of Si-O, Co-O, C-C, C-O, C=O linkages as indicated by Lorentzian-Gaussian curve fitting of the atom pairs (cf. text)

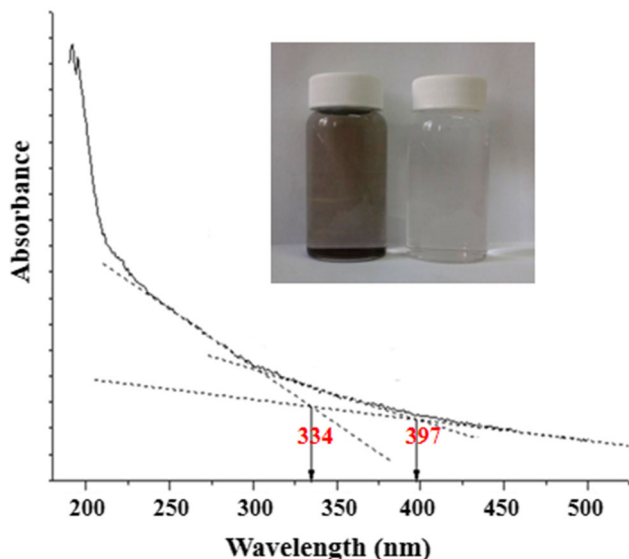


Fig. 14 UV-visible absorption spectrum of the colloidal suspension containing particulates/condensates (mainly Si-H-doped Co_{1-x}O and minor LDH, graphene and graphite) produced by PLA of Co in TEOS for 5 min (left bottle). The bottle with pure TEOS is also inset

can be extended to the synthesis of $(\text{Co}/\text{CoO})_n$ multilayer for magnetoelectronics applications. It is also an open question whether the C-Si-H-doped cobalt oxides with (hkl)-specific defects and UV-visible absorbance (3.1–3.7 eV) under the

influence of carbonaceous substances can have useful optocatalytic applications.

Acknowledgments This research was supported by Center for Nanoscience and Nanotechnology at NSYSU and partly by the Ministry of Science and Technology, Taiwan (ROC).

References

1. W.H. Lee, P. Shen, *J. Solid State Chem.* **177**, 101 (2014)
2. M.Y. Li, P. Shen, *Mater. Sci. Eng. B* **111**, 82 (2014)
3. T.M. Tsai, K.C. Yang, P. Shen, *J. Solid State Chem.* **177**, 3301 (2004)
4. C.N. Huang, P. Shen, K.Y. Hsieh, *J. Eur. Ceram. Soc.* **27**, 4685 (2007)
5. C.N. Huang, S.Y. Chen, M.H. Tsai, P. Shen, *J. Cryst. Growth* **305**, 285 (2007)
6. B.Y. Chen, S.S. Lin, P. Shen, S.Y. Chen, *CrystEngComm.* **17**, 4919 (2015)
7. B.Y. Chen, S.S. Lin, P. Shen, S.Y. Chen, *CrystEngComm.* **17**, 8307 (2015)
8. S. Hu, C. Melton, D. Mukherjee, *Phys. Chem. Chem. Phys.* **2014**(16), 24034 (2014)
9. B.C. Lin, P. Shen, S.Y. Chen, *J. Nanoparticle Res.* **16**, 2444 (2014)
10. C.H. Wu, S.Y. Chen, P. Shen, *CrystEngComm.* **16**, 2220 (2014)
11. C.H. Wu, S.Y. Chen, P. Shen, *Carbon* **67**, 27 (2014)
12. M.N. Baibich, J.M. Broto, A. Fert, F. Nguyen van Dau, F. Petroff, P. Eitenne, G. Creuzet, A. Friederich, J. Chazelas, *Phys. Rev. Lett.* **61**, 2472 (1988)

13. G. Binasch, P. Grünberg, F. Saurenbach, W. Zinn, *Phys. Rev. B* **39**, 4828 (1989)
14. J.F. Moulder, W.F. Stickle, P.E. Sobol, K.D. Borben, *Handbook of X-ray Photoelectron Spectroscopy* (Physical Electronics, Inc, USA, 1995)
15. C.W. Tang, T.Y. Leu, W.Y. Yu, C.B. Wang, S.H. Chien, in *83th Annual Academic Conference of Chinese Military Academy*, CH-18-26, June 1, 2007, Fengshan, Kaohsiung, Taiwan, ROC
16. C.C. Lin, P. Shen, J. Noncrystal. Solids **171**, 281 (1994)
17. F. Rubio, J. Rubio, J.L. Oteo, *Spectrosc. Lett.* **31**, 199 (1998)
18. N. Mansour, A. Momeni, R. Karimzadeh, M. Amini, *Optic. Mater. Express* **2**, 740 (2012)
19. H. Gao, G. Wang, M. Yang, L. Tan, J. Yu, *Nanotechnology* **23**, 015607 (2012)
20. S. Kundu, M.D. Mukadam, S.M. Yusuf, M. Jayachandran, *CrystEngComm* **15**, 482 (2013)
21. M.C. Biesinger, B.P. Payne, A.P. Grosvenor, L.W.M. Lau, A.R. Gerson, R.S.C. Smart, *Appl. Surf. Sci.* **257**, 2717 (2011)
22. A. Foelske, H.H. Strehblow, *Surf. Interface Anal.* **29**, 548 (2000)
23. J.C. Dupin, D. Gonbeau, H. Benqlilou-Moudden, P. Vinatier, A. Levasseur, *Thin Solid Films* **384**, 23 (2001)
24. A.P. Grosvenor, S.D. Wik, R.G. Cavell, A. Mar, *Inorg. Chem.* **44**, 8988 (2005)
25. M. Oku, Y. Sato, *Appl. Surf. Sci.* **55**, 37 (1992)
26. A.R. Remsberg, R.C. Liebermann, *Phys. Chem. Miner.* **18**, 161 (1991)
27. L.G. Liu, W.A. Bassett, *Elements, Oxides, and Silicates: High-Pressure Phases with Implications for the Earth's Interior* (Oxford University Press, Oxford, 1986)
28. F.A. Kröger, H.J. Vink, *Solid State Phys.* **3**, 307 (1956)
29. C.B. Ma, *J. Geophys. Res.* **79**, 3321 (1974)
30. H. Horiuchi, M. Akaogi, H. Sawamoto, adsf, in *Advances in Earth and Planetary Sciences 12, High-pressure Research in Geophysics*, ed. by S. Akimoto, M.H. Manghnani (Centre for Academic Publications, Tokyo, 1982), p. 391
31. P.T. Chao, P. Shen, S.L. Hwang, *Mater. Sci. Eng. A* **112**, 233 (1989). **(and references therein)**
32. V. Krasevec, *Mater. Res. Bull.* **9**, 1357 (1974)
33. P. Shen, *Microstructure of josephinite revealed by transmission electron microscope*, M.S. Thesis, Cornell University, 1982
34. W.A. Deer, R.A. Howie, J. Zussman, *An Introduction to the Rock-Forming Minerals*, 2nd edn. (Longman Scientific Technical, Essex, 1992)
35. A. Putnis, *Introduction to Mineral Sciences* (Cambridge University Press, Cambridge, 1992), p. 457
36. B.C. Lin, C.N. Huang, P. Shen, S.Y. Chen, *CrystEngComm* **16**, 1459 (2014)
37. C.J. Quinn, D.L. Kohlstedt, *J. Am. Ceram. Soc.* **67**, 305 (1984)
38. K.J. Cai, Y. Zheng, P. Shen, S. Chen, *CrystEngComm* **16**, 5466 (2014)
39. S.S. Lin, S.Y. Chen, P. Shen, *CrystEngComm* **17**, 4937 (2015)
40. J.J. Papike (Ed.) *Planetary Materials, Reviews in Mineralogy*, volume 36, ed. P.H. Ribbe (Mineralogical Society of America, Washington, 1998)
41. J.A. Katine, F.J. Albert, R.A. Buhrman, *Phys. Rev. Lett.* **84**, 3149 (2000)
42. F.J. Albert, J.A. Katine, R.A. Buhrman, *Appl. Phys. Lett.* **77**, 3809 (2000)
43. S. Yuasa, A. Fukushima, T. Nagahama, K. Ando, Y. Suzuki, *Jpn. J. Appl. Phys.* **43**, L588 (2004)
44. S. Yuasa, T. Nagahama, A. Fukushima, Y. Suzuki, K. Ando, *Nat. Mater.* **3**, 868 (2004)
45. S.S.P. Parkin, C. Kaiser, A. Panchula, P.M. Rice, B. Hughes, M. Samant, S.H. Yang, *Nat. Mater.* **3**, 862 (2004)